Widefield and high-resolution reflectance imaging of gold and silver nanospheres

Nitin Nitin*
David J. Javier*
Darren M. Roblyer
Rebecca Richards-Kortum
Rice University
Department of Bioengineering
6100 Main Street
Keck Hall, Suite 116
Houston, Texas 77005

Abstract. Metallic nanoparticles have unique optical properties that can be exploited for molecular imaging in tissue. Image contrast depends on the nature of the particles, properties of the target tissue, and the imaging system. Maximizing image contrast for a particular application requires an understanding of the interplay of these factors. We demonstrate an approach that integrates the use of reflectance spectroscopy and imaging of particles in water and various tissue phantoms to evaluate the expected image contrast. We illustrate the application of this methodology for gold and silver nanospheres targeted against a biomarker expressed in epithelial tissue; predictions of contrast properties using diffuse reflectance spectroscopy were compared with widefield and high-resolution images of labeled tissue phantoms. The results show that the predicted image contrast based on spectroscopy agrees well with widefield and high-resolution imaging, and illustrate that gold and silver nanospheres at subnanomolar concentration are sufficient to produce contrast in both imaging modes. However, the effective contrast achieved with a particular type of nanoparticle can differ dramatically depending on the imaging modality. The ability to predict and optimize image contrast properties is a crucial step in the effective use of these nanomaterials for biomedical imaging applications.
[DOI: 10.1117/1.2800314]

Keywords: metallic nanoparticles; reflectance spectroscopy; gold and silver nanospheres; molecular imaging; widefield imaging; confocal imaging.

Paper 07002SSR received Jan. 3, 2007; revised manuscript received Aug. 7, 2007; accepted for publication Sep. 14, 2007; published online Nov. 1, 2007.

1 Introduction

For decades, metal nanoparticles such as colloidal gold and silver have been used as contrast agents for electron microscopy (EM) of biological specimens.[1,2] Recently, the enhanced localized surface plasmon resonance (LSPR) of metal nanoparticles has been exploited to develop optical sensors for *in vitro* biological assays.[3–8] As a result of the LSPR, gold- and silver-based metal nanoparticles exhibit significantly higher extinction coefficients than organic fluorophores.[9] Metal nanoparticles have unique absorption and scattering properties, which are strongly dependent on particle size, shape, material, and interparticle spacing. Most of the current bioassays that utilize metal nanoparticles rely on substantial changes in the color and strength of nanoparticle absorption upon target-induced aggregation.[9–11]

More recently, a number of studies have suggested that light scattering from targeted gold nanoparticles can be used to image changes in biomarker expression in living biological specimens, including cell culture[12–14] and fresh human tissue explants.[15] *In vivo* molecular-specific reflectance imaging using targeted metal nanoparticles offers important advantages for point-of-care detection of disease; metal nanoparticles resonantly scatter light with distinct spectral features[14–16] and backscattered light can be collected from optically thick biological specimens. The scattering cross-section of metal nanoparticles is several orders of magnitude larger than that of polymeric particles of similar size.[14] The scattering signal from a single nanoparticle has been shown to be equivalent to $\sim 10^6$ fluorophores in a homogeneous assay[6,9] and is not affected by photobleaching, providing the potential for these nanoparticles to detect biological molecules at very low concentrations over long periods of time. Theoretical calculations suggest that light scattering can be detected from as low as 10^{-16} M concentration of nanoparticles in solution.[17,18] Furthermore, several studies suggest that metal nanoparticles can be safely delivered *in vivo* for diagnostic imaging applications. Metallic gold and silver nanoparticles have shown low bioreactivity and toxicity.[19–21]

Recent developments in photonic technology provide the ability to noninvasively image cellular morphology *in vivo*; the use of optically active metal nanoparticles provides an opportunity to simultaneously image cellular morphology and changes in biomarker expression with subcellular spatial resolution. For many diagnostic applications, it is desirable to combine high-resolution imaging with low-resolution wide-

*Contributed equally to this manuscript.
Address all correspondence to Rebecca Richards-Kortum, PhD, Department of Bioengineering, Rice University, 6100 Main Street, Houston, TX 77005; Tel: 713–348–5869; Fax: 713–348–5877; E-mail: rkortum@rice.edu

1083-3668/2007/12(5)/051505/10/$25.00 © 2007 SPIE

field imaging. The ability to initially interrogate large areas of suspicious tissue with widefield imaging, followed by high-resolution imaging of suspicious regions, has the potential to improve the sensitivity and specificity of disease detection. A number of simple surgical microscopes and endoscopes that can capture multispectral digital images of large areas of tissue in real time have recently been developed to survey large surface areas of tissue and identify suspicious regions of interest. These areas can then be imaged with higher spatial resolution using high-resolution chromoendoscopy, optical coherence tomography, or *in vivo* confocal microscopy to achieve subcellular image resolution in near real time to confirm the presence of disease.[22,23]

Targeted contrast agents can enhance image contrast in both modalities; however, the production of image contrast in widefield and high-resolution optical imaging differs. In widefield imaging, detected photons can undergo multiple scattering events and image contrast is produced as a result of local fluctuations in both light scattering and absorption. On the other hand, high-resolution reflectance imaging relies predominantly on single backscattering to generate image contrast. An ideal molecular-targeted contrast agent should provide significant contrast in both widefield and high-resolution imaging modes at physiologically relevant concentrations of target biomarkers.

Image contrast depends on a number of factors, including the optical properties of the particles themselves, the properties of the target tissue including the baseline optical properties and the concentration of the targeted biomarker concentration, as well as properties of the system used to acquire images. Maximizing image contrast for a particular application requires an understanding of the interplay of these factors. A number of theoretical approaches have been developed to predict the absorption and scattering properties of single metallic nanoparticles as a function of their size, shape, and material composition.[24,25] These studies have provided insights into how changes in particle design affect the optical properties of single particles, but they do not fully address the important question of the expected image contrast when a particular particle is used as a contrast agent in biological tissue.

In this paper, we describe a methodology to evaluate expected image contrast as a function of particle optical properties, tissue optical properties, and imaging modality. We illustrate the application of this methodology to predict image contrast for gold and silver nanospheres targeted against a biomarker expressed in epithelial tissue in both widefield and high-resolution imaging modalities. Predictions based on diffuse reflectance spectroscopy are compared with experimental results of widefield and high-resolution images of labeled tissue phantoms. Predictions of image contrast agree well with those observed experimentally. Results illustrate the potential of gold and silver nanospheres to produce significant contrast in both widefield and high-resolution imaging at subnanomolar concentration. Interestingly, image contrast for a particular particle can differ dramatically for widefield and high-resolution reflectance imaging.

The goal of this study is to develop and evaluate a method to predict the anticipated image contrast properties of targeted gold and silver nanospheres in widefield and high-resolution imaging for biomedical imaging applications. This basis of this method is the use of diffuse reflectance spectroscopy to evaluate the remitted light from nanoparticles as a function of both the optical properties of the surrounding environment and any biomarker induced aggregation of targeted nanoparticles.[26] We illustrate that image contrast in both high-resolution imaging and widefield imaging can be predicted by measuring diffuse reflectance spectra of nanoparticles in a variety of phantoms of progressively increasing complexity, including water, turbid gelatin, and cell-culture-based tissue phantoms. Reflectance spectra of nanoparticles in water provide a measure of their scattering in a dilute suspension and can predict image contrast anticipated in high-resolution reflectance imaging. Reflectance spectra of nanoparticles in gelatin and cell-culture-based tissue phantoms provide a measure of their expected image contrast in widefield reflectance imaging. Gelatin phantoms provide a simple model, which mimics the extracellular environment of a tissue without any contribution from cells, while cell-based tissue phantoms model both the cellular and extracellular environment of a tissue. To validate the predictions of this method, we present experiments that compare contrast predicted based on diffuse reflectance spectroscopy measurements directly to that achieved in both high-resolution and widefield reflectance images.

For the results of this methodology to be applicable to biomedical imaging, it is important to choose both the size and concentration of contrast agents to be biologically relevant. For biomedical imaging applications, the size range of nanoparticles is often determined based on the potential for effective *in vivo* delivery to a target tissue. Using various delivery routes, molecular imaging applications have successfully used nanoparticles in the size range of 20 to 100 nm in diameter.[26,27] Larger sized nanoparticles are not effective for targeting deep within a tissue, while small-sized particles (1 to 15 nm) do not have a high scattering cross section.[28] Thus, in this study we focused on gold and silver nanospheres with a mean diameter of 50 nm as a representative size to determine the contrast properties of these particles. In addition, experiments were also carried out with 25-nm gold nanoparticles, to evaluate the effect of size on contrast properties of nanoparticles.

In many molecular imaging applications, the target biomarker is often present at low concentration, often at subnanomolar levels. Thus, in phantoms lacking cells we used subnanomolar concentrations of particles. In cell-culture-based phantoms, we targeted the epidermal growth factor receptor (EGFR); in these phantoms, the total number of EGFR receptors determines the maximum concentration of nanoparticles. For phantoms containing approximately 30 million cancer cells per ml with an estimated 10^5 EGFR receptor molecules per cell[29] and assuming a 100% efficiency of targeting, the effective concentration of nanoparticles in a tissue phantoms is still below the nanomolar level. Thus, the contrast properties of nanoparticles in this study were evaluated at a subnanomolar level of concentration in all model systems.

2 Material and Methods

2.1 *Materials*

High-purity (>99%) chemicals for nanoparticle synthesis [sodium citrate, gold chloride ($HAuCl_4$) and silver nitrate

($AgNO_3$)] were purchased from Sigma-Aldrich, St. Louis, Missouri. $HAuCl_4$ and $AgNO_3$ were purchased with >99.999% purity and stored in the dark under desiccating conditions. In this study, the SiHa cell line was used as a model system to target the EGFR. The SiHa cell line was purchased from ATCC, Manassas, Virginia. Nanoparticles were targeted using antibodies purchased from Sigma; anti-EGFR (clone 29.1, Sigma) was used as positive control and anti-IgG (clone UPC-10, Sigma) was used as a negative control.

2.2 *Methods*

2.2.1 *Synthesis and characterization of nanoparticles*

For synthesis of gold nanospheres, we used the sodium citrate reduction of gold ions developed by Frens.[30] Nanosphere size was controlled by adjusting the ratio of Au ions ($HAuCl_4$) and sodium citrate. The size of the particles was analyzed using transmission electron microscopy (TEM) (JEOL 2010, Tokyo, Japan) and dynamic light scattering (DLS, Brookhaven Instruments Corp., Holtsville, New York). The citrate reduction procedure was tailored to produce a highly monodisperse gold nanoparticles of both 50 ± 5 nm and 25 ± 2 nm diameter (data not shown). Comparison of TEM and DLS results for gold nanospheres showed good agreement for measurements of particle diameter, with results agreeing within 10%.

For synthesis of silver nanospheres, we adapted a process originally proposed by Lee and Meisel.[31] and further modified by Pillai and Kamat.[32] This process is analogous to the synthesis of gold nanoparticles wherein Ag ions are reduced using sodium citrate. For this synthesis, we used a 1:5 ratio of Ag:citrate ions. The size of the nanoparticles was also analyzed using TEM and DLS; a more polydisperse population of silver nanoparticles was obtained (50 ± 15 nm). Due to the relatively large heterogeneity in size of silver nanoparticles, we limited our study of silver nanoparticles to those with a 50-nm mean diameter.

The concentration of gold and silver nanoparticles was determined using a combination of inductively coupled plasma atomic emission spectroscopy (ICP-AES) with theoretical calculations based on particle size, density, molecular weight, and packaging of atoms in nanospheres. Using ICP-AES, we determined the concentration of gold or silver atoms in solution; this result was used together with theoretical calculations of the number of atoms per nanoparticle to determine the concentration of nanoparticles in solution. Prior to concentration measurements with ICP-AES, the solution of nanoparticles was centrifuged to remove free atoms of gold or silver in the solution. Based on this measurement and calculation, the concentration of 50-nm-diameter gold and silver nanoparticles used in subsequent experiments was determined to be approximately 0.4 nM and 0.07 nM, respectively (data not shown). This subnanomolar concentration of nanoparticles was used in all experiments in this study.

2.2.2 *Bioconjugation of antibodies with nanoparticles*

For molecular targeting of nanoparticles, we conjugated antibodies to the surface of the synthesized nanoparticles. In these experiments we used the anti-EGFR antibody as a positive control and a nonspecific anti-IgG as a negative control. Antibodies were directly conjugated using the protocol reported by Sokolov et al.[14] Briefly, the antibody was incubated with nanoparticles for approximately 30 min in a salt-free environment. After incubation, nanoparticles were centrifuged to remove excess antibodies in the presence of 1% PEG (10,000 MW). After centrifugation and decantation of solution, the pellet of nanoparticles was dispersed in 1X PBS and tested for colloidal stability using the conventional salt test. In this test, the nanoparticle solution was tested using 10% NaCl solution and stability was determined by visual assessment of color change. In the case of antibody-coated particles, we did not observe any color change, indicating colloidal stability based on this salt test procedure.

2.2.3 *Diffuse reflectance spectroscopy*

To assess the potential image contrast available in widefield and high-resolution imaging modes, we measured extinction and diffuse reflectance spectra of nanoparticles in various model systems of increasing complexity and relevance to tissue imaging. These model systems included particles in suspension in water, particles embedded in turbid gelatin which mimics the scattering of tissue stroma, and particles targeted to biomarkers expressed in cell-culture-based tissue phantoms. Transmission and diffuse reflectance spectra were measured from these samples using a Cary 5000 spectrometer; for diffuse reflectance measurements, the device was equipped with an integrating sphere to collect diffuse backscattered light. Transmission spectra were measured from 350 to 800 nm, while reflectance spectra were measured from 400 to 800 nm. To remove any contribution from the specular reflection of light, the integrating sphere was adjusted so that only diffusely scattered light was collected.

Extinction spectra and diffuse reflectance spectra were measured from an aqueous solution of nanoparticles in water, prepared from a threefold dilution of stock solution of nanoparticles (as synthesized). Diffuse reflectance spectra were also measured from a solution of nanoparticles embedded in gelatin. These samples were prepared by suspending a threefold dilution of the stock solution of nanoparticles in 10% gelatin. Finally, diffuse reflectance spectra were measured from a tissue phantom containing approximately 30 million SiHa cells/ml, labeled with anti-EGFR conjugated nanoparticles, embedded in 10% gelatin. In each case, spectra were measured from an appropriately matched control sample containing no nanoparticles. Spectra of model phantoms with nanoparticles are reported relative to the appropriate blank containing all the same materials except the nanoparticles. The relative scattering or absorption of model phantoms was evaluated based on a ratio of diffuse reflectance signal from model phantoms with nanoparticles as compared to its appropriate blank at each wavelength value ranging from 350 to 800 nm.

2.2.4 *Optical properties of gelatin and tissue phantoms*

To compare the optical properties of gelatin and tissue phantoms with those of epithelial tissues, scattering and absorbance properties of model phantoms were measured. The attenuation coefficient of gelatin and tissue phantoms was determined by fitting the depth-dependent confocal reflec-

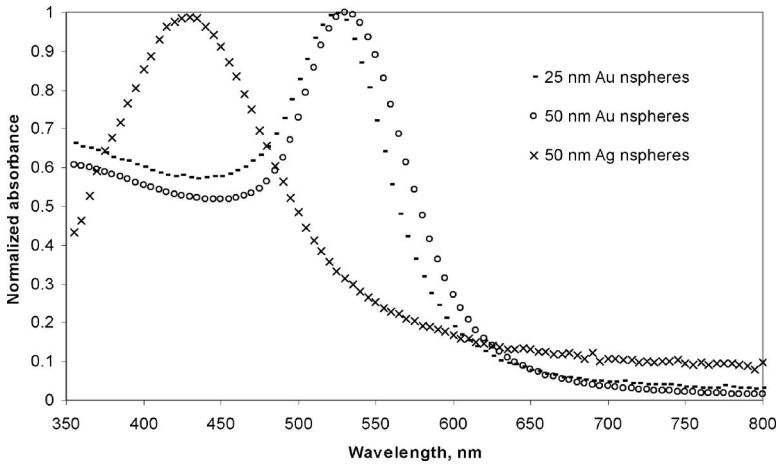

Fig. 1 UV-Vis spectra of gold and silver nanospheres. The peak absorption of silver (Ag nanospheres of 50-nm mean diameter) and gold nanospheres (Au nanospheres of 25- and 50-nm diameters) is ~430 and ~530 nm, respectively.

tance intensity measured at 830 nm to an exponential function of depth, based on Beer's law of attenuation.[33] Using this approach, the attenuation coefficients for gelatin and tissue phantoms were estimated to be approximately 6 and 60 cm^{-1}, respectively. The attenuation coefficient of tissue phantoms are comparable to results obtained for cervical epithelium.[33] (~60–120 cm^{-1}). The absorbance coefficient was experimentally measured for liquid gelatin phantoms (scattering is negligible in liquid form) using UV-Vis measurement. Based on this measurement, the absorbance coefficient was estimated to be 0.6 cm^{-1}. Thus, the optical properties of the tissue phantoms used here mimic the epithelial environment, while gelatin phantoms have optical properties in between that of water and epithelial tissue.

2.2.5 *Widefield imaging using multispectral digital microscope*

To evaluate whether the image contrast predicted using diffuse reflectance spectroscopy can be translated to a clinically relevant imaging setup, we carried out experiments to assess image contrast in both high-resolution and widefield reflectance imaging modes. Widefield multispectral reflectance imaging was performed on samples of nanoparticles in different environments including both gelatin and tissue phantoms. Images were obtained using a multispectral digital microscope (MDM) with a field of view greater than 1 cm. The MDM incorporates a broadband light source and narrowband illumination filters to capture reflectance images at multiple illumination wavelengths (450, 530, 600, and 650 nm) and also using white-light illumination. These wavelengths were selected based on spectral characteristics of nanoparticles in diffuse reflectance spectroscopy and represent wavelengths with peak absorption and scattering contrast noted within the reflectance spectra. Exposure times were kept constant between samples at each illumination wavelength to allow for quantitative signal comparison. The image intensity at each wavelength was normalized to that from pure gelatin or tissue phantoms without added contrast agents. A black anodized aluminum plate was used as a low-reflectance background for imaging.

2.2.6 *High-resolution confocal reflectance imaging*

To demonstrate the specificity of molecular targeting with nanoparticle-based contrast agents, nanoparticles coated with antibodies for EGFR and IgG were incubated with cells in suspension at 37°C for 30 min. Incubation of IgG-coated nanoparticles with cells provides a negative control to determine the specificity of targeting. After incubation, cells were washed three times and centrifuged to remove unbound contrast agents. The resulting cell pellet was used to assess image contrast available in high-resolution confocal reflectance imaging. Cells were imaged using a Zeiss LSM 510 confocal microscope in reflectance mode. A 633-nm laser excitation was used for imaging gold and silver nanoparticles in reflectance mode.

To compare predicted image contrast from diffuse reflectance spectroscopy with high-resolution imaging, we imaged the molecular targeted contrast agents at multiple wavelengths (488, 533, and 633 nm) using confocal microscopy (Zeiss LSM 510). The wavelength values of 488, 543, and 633 nm approximately correspond to the peak contrast wavelengths for gold and silver nanoparticles based on diffuse reflectance spectroscopy (530 nm represents scattering peak for silver and absorption peak for gold nanoparticles, 633 nm represents a scattering maxima for gold nanoparticles). Standard laser lines available in the Zeiss confocal system limited our choice of wavelengths for characterizing the wavelength response of the nanoparticles.

3 Results and Discussion

3.1 *Characterization of Gold and Silver Nanospheres*

Figure 1 shows UV-Vis extinction spectra of gold (50 nm, 25 nm) and silver nanoparticles (50 nm) in water. In each case, spectra are normalized to a peak extinction value of 1. Solutions of silver nanospheres are light yellowish in color and exhibit peak extinction at approximately 430 nm, while solutions of gold nanospheres are deep red in color with peak extinction at approximately 530 nm. The extinction peak of gold nanoparticles does show a slight shift with a change in size from 25 to 50 nm. The peak extinction value for

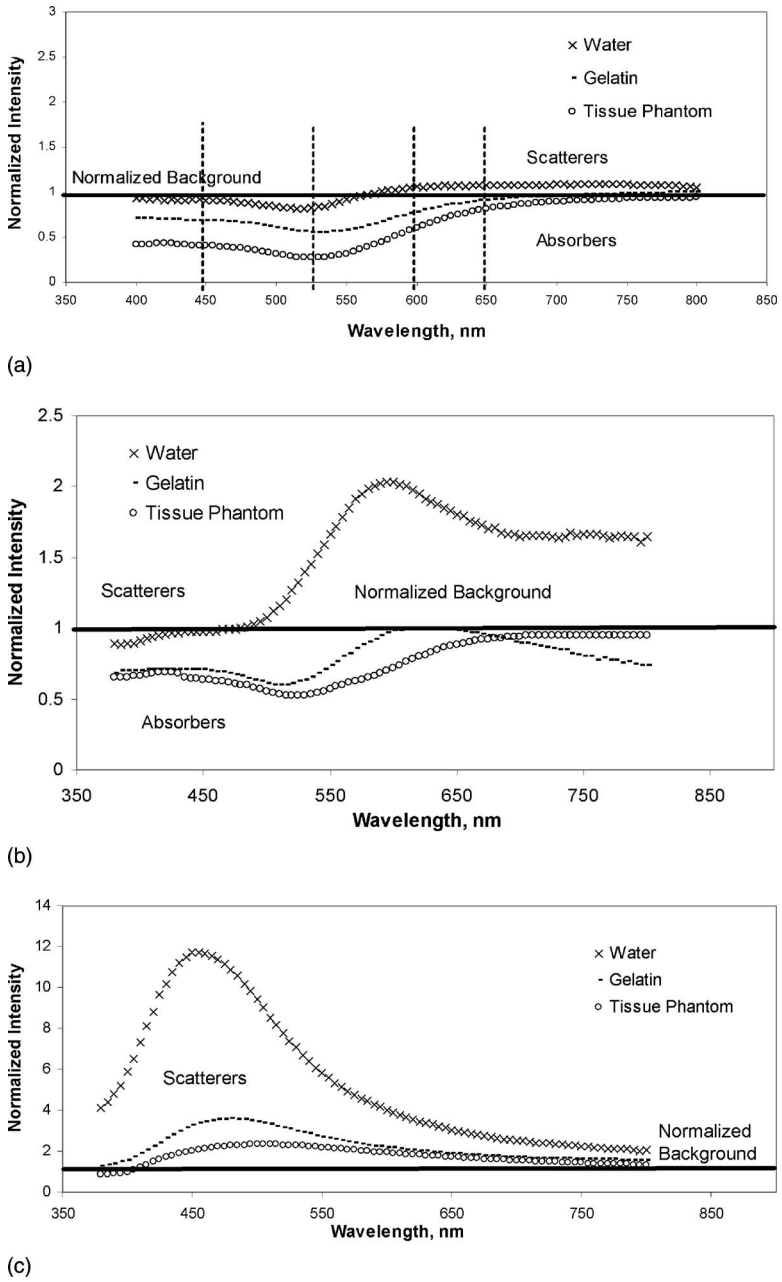

Fig. 2 Diffuse reflectance spectroscopy of (a) 25-nm gold (b) 50-nm gold, and (c) 50-nm silver nanoparticles in water, gelatin, and molecular targeted tissue phantoms.

25-nm-diameter particles is 524 nm, while that for 50-nm-diameter particles is observed at 529 nm.

3.2 *Diffuse Reflectance Spectroscopy of Gold and Silver Nanospheres in Model Phantoms*

Figure 2 shows the diffuse reflectance spectra from nanoparticles in three model systems: water, gelatin, and a tissue phantom. In each case, the spectra shown are divided pointwise by that measured from a blank of identical composition except for the nanoparticles. Thus, relative signal intensity greater than 1 indicates that the particles are expected to provide positive image contrast whereas values lower than 1 predicts absorptive contrast. The spectra measured in aqueous suspension are predominantly governed by single scattering, and can be used to predict contrast expected in high-resolution reflectance imaging, while the data measured in gelatin and tissue phantoms include contributions from multiple scattering, and can be used to predict contrast expected in widefield reflectance imaging.

Figure 2(a) shows reflectance spectra measured for phantoms containing 25-nm-diameter gold nanospheres, Fig. 2(b) shows that for 50-nm gold nanospheres, and Fig. 2(c) shows results for 50-nm-diameter silver nanospheres. In water, the scattering of the subnanomolar concentration of 25-nm gold nanoparticles is only slightly higher than the background signal at wavelengths above 580 nm; below this wavelength,

contrast is predominantly absorptive even in suspension. In contrast, the diffuse reflectance spectra of the subnanomolar concentration of 50-nm-diameter nanospheres are significantly higher than that of the background at wavelengths above 500 nm. This can be explained based on the lower scattering coefficient of 25-nm nanoparticles as compared to 50-nm-diameter gold nanoparticles. In both gelatin and tissue phantoms, the diffuse reflectance of samples containing 25- and 50-nm nanoparticles is lower than that of the corresponding background with a maximal absorption around 530 nm. This suggests that these particles are expected to provide predominantly absorptive contrast in widefield imaging. Similar to the UV-Vis results, we did not observe a significant change in spectral characteristics as the particle size increases from 25 to 50 nm in diameter in gelatin and tissue phantoms.

Figure 2(c) shows the diffuse reflectance spectra of silver nanospheres in water, gelatin, and tissue phantoms, normalized to the appropriate background. Results demonstrate that silver nanoparticles provide positive contrast in all model systems, including tissue phantoms. This is consistent with the higher scattering coefficient expected of silver nanoparticles. The maxima of the scattering contrast from silver nanoparticles in gelatin and tissue phantoms occurs at approximately 500 to 550 nm, and is red-shifted relative to the diffuse reflectance peak at approximately 475 nm observed in water. Determination of these shifts in peak wavelength is important to optimize contrast properties of nanoparticles for biomedical imaging.

3.3 *Widefield Imaging of Gold and Silver Nanospheres in Model Phantoms*

In order to evaluate the predictions based on Fig. 2, we obtained widefield reflectance images of nanospheres in gelatin phantoms at several illumination wavelengths. Results are shown in Fig. 3. Figure 3(a) shows widefield reflectance images of 50-nm-diameter gold and silver nanospheres in gelatin phantoms, as well as control images of gelatin phantoms without nanoparticles. The images are collected using same exposure time at each particular wavelength range. Figure 3(b) shows the normalized average intensity of measured from the nanoparticle containing phantom relative to that of the gelatin blank at each illumination wavelength. Figure 3(b) indicates that the contrast produced by the 50-nm gold nanospheres is absorptive (less than 1) at illumination wavelengths below 600 nm; this is consistent with the predictions of diffuse reflectance measurements in gelatin. Based on multispectral imaging, the peak absorptive contrast from gold nanoparticles is obtained at 530 nm. The contrast produced the silver nanospheres is positive at all wavelengths, with peak contrast measured at 530-nm illumination. These results illustrate that these materials can provide both absorptive and scattering based contrast. The nature and wavelength dependence of contrast in widefield imaging are predicted well by diffuse reflectance measurements in gelatin-based phantoms.

Figure 4(a) shows widefield images of molecular targeted contrast agents in tissue phantoms using multispectral widefield imaging as well as images from an unlabeled tissue phantom. In these tissue phantoms, gold or silver nanospheres (50-nm mean diameter) conjugated with anti-EGFR antibodies were targeted to SiHa cells, which after removal of excess contrast agents were added to gelatin solution to form tissue phantoms. Figure 4(b) shows the normalized mean reflectance intensity of phantoms containing molecular targeted contrast agents relative to the signal from the unlabeled control tissue phantom. The results indicate that tissue phantoms labeled with gold nanospheres produce primarily absorptive contrast at all illumination wavelengths examined in widefield imaging. Again, results agree well with diffuse reflectance spectroscopy measurements in tissue phantoms. Phantoms labeled with molecular targeted silver nanoparticles show positive contrast at all wavelengths, with peak contrast observed at 530-nm illumination.

In many widefield-imaging applications, an intensity ratio of approximately 3 units is considered a significant contrast. Based on the literature, studies with fluorescence molecular imaging using IR and near-IR labels[34,35] have reported intensity ratios ranging from 1.2 to 3.0. This ratio is achievable only with selection of an optimized wavelength range. In other imaging modalities such as MR imaging, intensity ratios above 1.5 are considered as a strong signal.[36]

3.4 *Contrast Properties of Nanospheres Using High-Resolution Imaging*

Figure 5(a) shows high-resolution confocal reflectance images of cells labeled with targeted gold and silver nanospheres obtained at 633-nm illumination. Confocal reflectance images were obtained from cells targeted with anti-EGFR conjugated nanoparticles; IgG conjugated nanoparticles were used a negative control to assess specificity of targeting. The images show an increase in perimembrane reflectance in EGFR labeled cells, with some intracellular signal; this intracellular signal could result from internalization of targeted receptors. The results demonstrate specific targeting of nanoparticle-based contrast agents. Additionally, the results show positive contrast from both anti-EGFR targeted gold and silver nanoparticles, and are consistent with the results of the diffuse reflectance spectra measured in water.

Figure 5(b) shows high-resolution confocal reflectance images of cells labeled with gold and silver nanoparticles as the illumination wavelength is varied from 633 to 533 to 488 nm. Based on the gray-scale intensity of image contrast at each wavelength, we calculated ratiometric contrast of silver to gold as 0.93 at 633 nm, 3.0 at 533 nm, and 3.98 at 488 nm. The results agree well with diffuse reflectance spectra measured in water and show that gold-nanoparticle-based molecular contrast agents provide strongest scattering contrast at 633 nm, while their contrast at 488- and 533-nm excitation is significantly lower. For silver-nanoparticle-based molecular contrast agents, strong positive contrast is observed across a broad range of wavelengths showing high peaks at 488 and 533 nm. The results of multiwavelength high-resolution imaging of contrast agents are in agreement with the predicted contrast based on diffuse reflectance spectroscopy of gold and silver nanoparticles in water.

4 Summary and Conclusion

In summary, we have demonstrated an approach to help predict the effective image contrast from exogenous nanoparticle-based contrast agents for biomedical imaging applications. This approach integrates spectroscopy, widefield

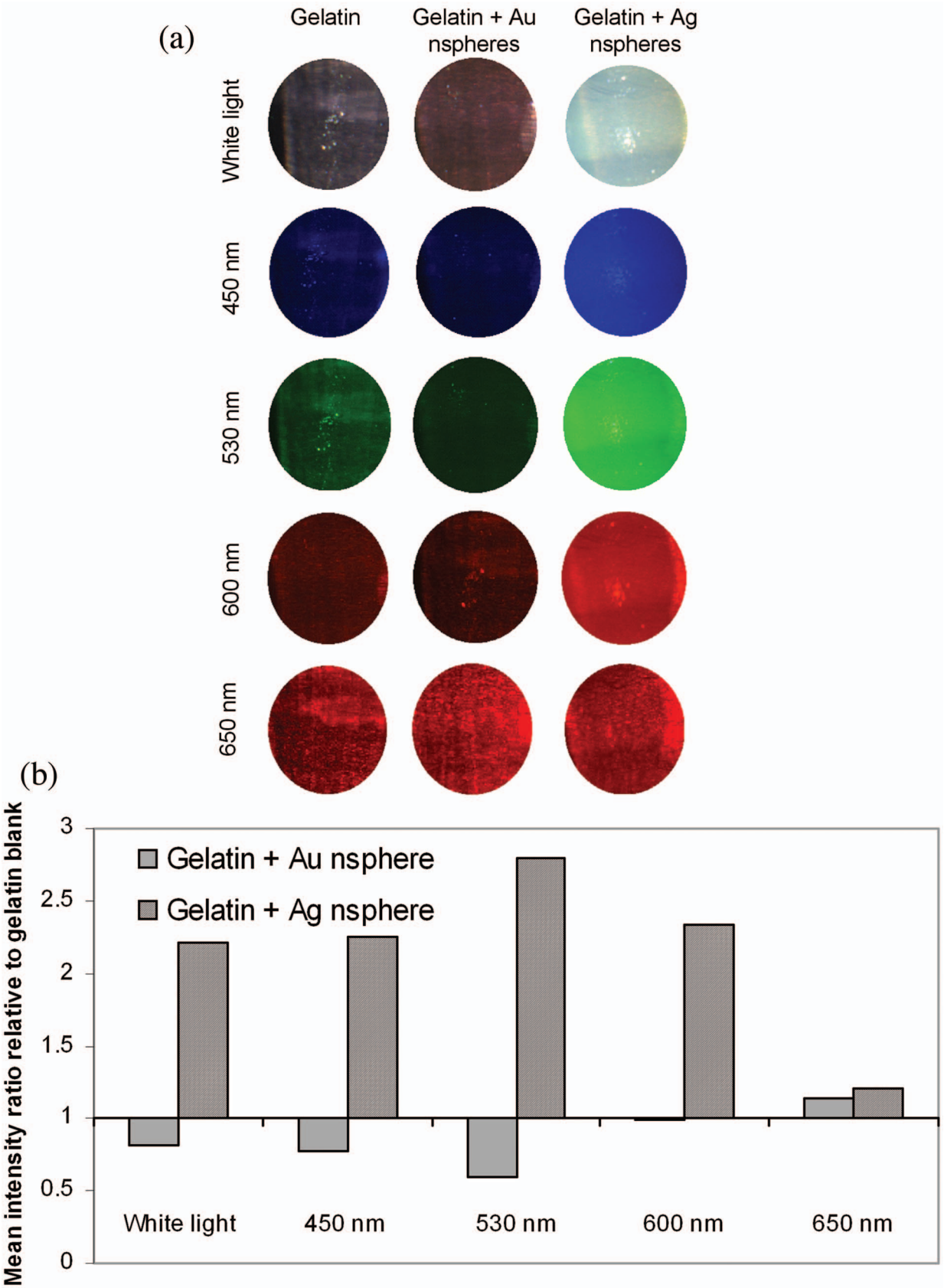

Fig. 3 (a) Widefield multispectral reflectance microscopy of gold and silver nanoparticles (50-nm mean diameter) in gelatin phantoms using white-light, 450-, 530-, 600-, and 650-nm excitation, respectively. (b) Normalized scattering intensity of gold and silver nanoparticles in gelatin phantoms. The intensity is normalized based on gelatin scattering (gelatin=1) at each excitation wavelength.

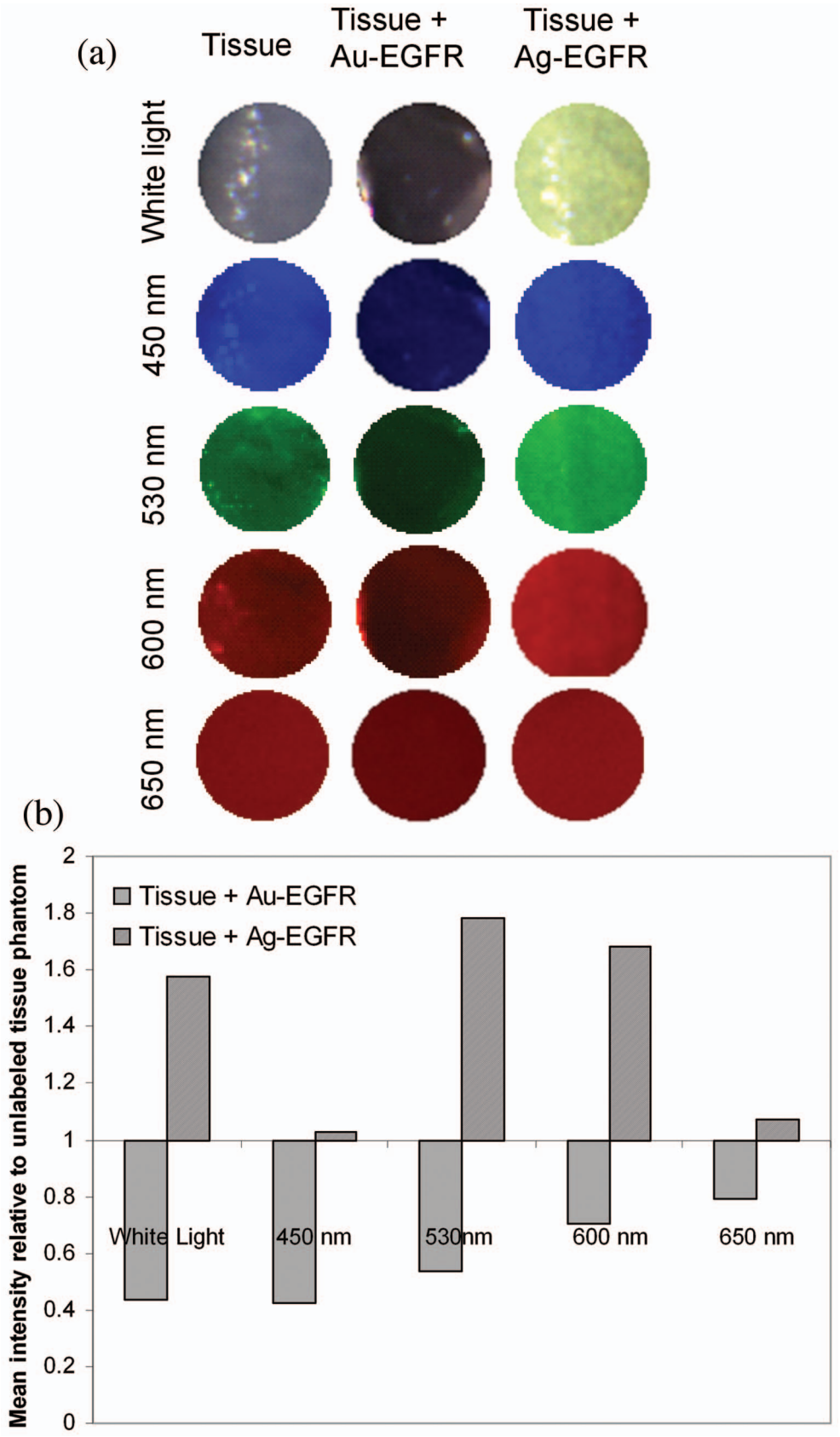

Fig. 4 (a) Widefield multispectral reflectance microscopy of gold and silver nanoparticles (50-nm mean diameter) in molecular targeted tissue phantoms using white-light, 450-, 530-, 600-, and 650-nm excitation, respectively. (b) Normalized scattering intensity of gold and silver nanoparticles in molecular targeted tissue phantoms. The intensity is normalized based on untargeted tissue phantom (untargeted tissue phantom=1).

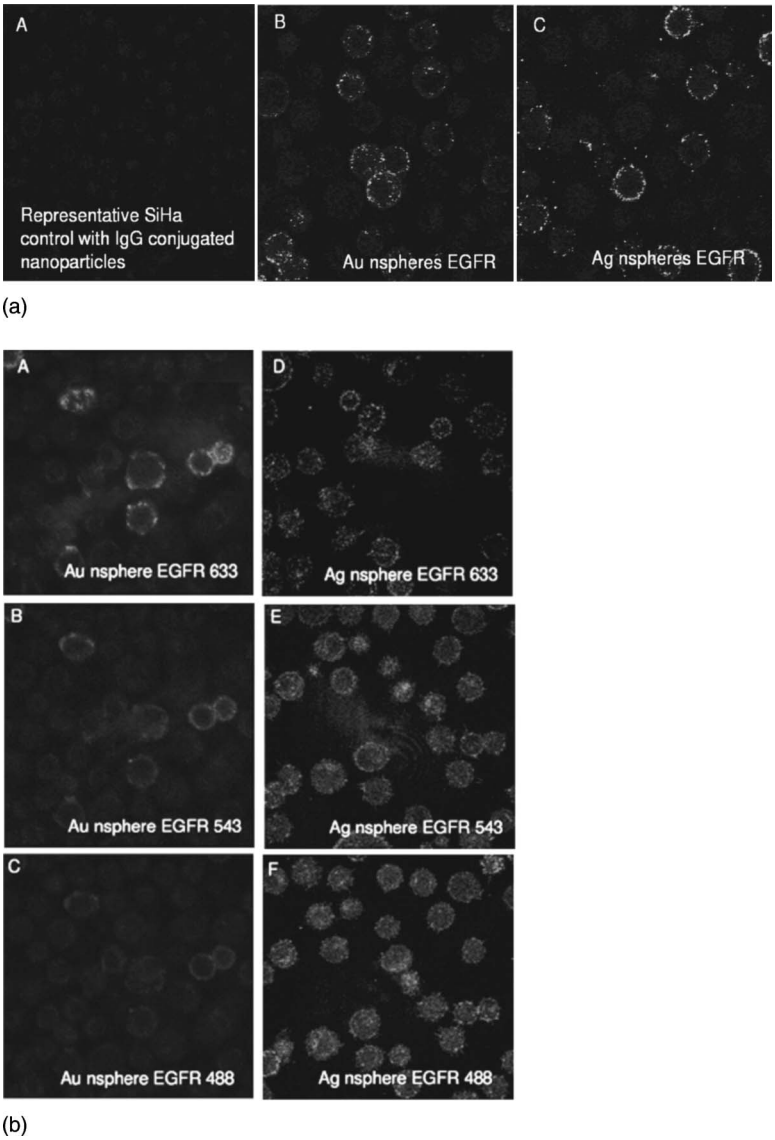

Fig. 5 (a) High-resolution imaging of gold and silver nanoparticles targeting EGFR receptors in cancer cells using confocal reflectance microscopy at 633-nm laser excitation: (A) representative IgG conjugated gold or silver nanoparticles as a negative control, (B) anti-EGFR conjugated gold nanoparticles, and (C) anti-EGFR conjugated silver nanoparticles. (b) Multispectral high-resolution confocal reflectance imaging of anti-EGFR targeted gold and silver nanospheres at 633-, 543-, and 488-nm laser excitation, respectively.

imaging, and high-resolution imaging to understand optimal contrast properties of nanoparticles as a function of nanoparticle size and composition, imaging modality, and surrounding environment. Contrast properties predicted from diffuse reflectance spectral measurements can provide an estimate of the effective image contrast as a function of these parameters. Using widefield and high-resolution imaging, the predicted contrast properties can be validated and optimal imaging wavelengths for maximizing the image contrast can be determined.

Based on this integrated approach, we demonstrate that gold and silver nanoparticles can provide a unique source of contrast for widefield and high-resolution imaging at subnanomolar concentration levels. Contrast properties of nanoparticles observed with diffuse reflectance spectroscopy were validated with multispectral widefield and high-resolution microscopy. While the nanoparticles investigated here can produce contrast either in diffuse reflectance mode for widefield imaging, or through single backscattering for high-resolution reflectance imaging, the resulting contrast depends strongly on both the imaging technique and the illumination wavelength, as well as the optical properties of the background medium. The results of diffuse reflectance spectroscopy and widefield imaging highlight that the expected image contrast from nanoparticle-based contrast agents is strongly dependent on the optical properties of the surrounding environment. This illustrates the need to evaluate the contrast properties of various nanomaterials in an appropriate biological environment.

Based on the results presented here, widefield reflectance imaging at 530-nm illumination provides an optimal operating point to achieve high contrast with both silver and gold

nanospheres, although the type of contrast is absorptive for gold nanospheres and scattering for silver nanospheres. For high-resolution imaging, gold nanoparticles provide peak scattering contrast at 633 nm while the peak scattering contrast for silver nanoparticles was observed at 543 nm.

Evaluating the contrast properties of nanoparticles in biologically relevant models is an important step in their translation from bench to bedside. Additional studies to develop efficient contrast agents will require development of novel coatings to improve stability and bioconjugation, noninvasive delivery and clearance routes for nanoparticles, and validation of their biocompatibility. These developments, in combination with engineering of novel instruments to detect specific contrast from nanoparticles, will enable the clinical translation of these technologies.

Acknowledgments

We thank Kenneth Dunner, Jr., and Cancer Center Core Grant CA16672 for TEM support, Vivian Mack for providing cell cultures, and BRP R01CA103830 (NCI).

References

1. J. Lloreta-Trull, L. Ferrer, T. Ribalta, et al., "Electron microscopy in pathology articles: a retrospective appraisal," *Ultrastruct. Pathol.* **24**(2), 105–108 (2000).
2. E. Suzuki, "High-resolution scanning electron microscopy of immunogold-labelled cells by the use of thin plasma coating of osmium," *J. Microsc.* **208**(Pt. 3), 153–157 (2002).
3. S. Eustis and M. A. El-Sayed, "Why gold nanoparticles are more precious than pretty gold: Noble metal surface plasmon resonance and its enhancement of the radiative and nonradiative properties of nanocrystals of different shapes," *Chem. Soc. Rev.* **35**(3), 209–217 (2006).
4. A. J. Haes and R. P. Van Duyne, "Preliminary studies and potential applications of localized surface plasmon resonance spectroscopy in medical diagnostics," *Expert Rev. Mol. Diagnost.* **4**(4), 527–537 (2004).
5. N. Nath and A. Chilkoti, "Label free colorimetric biosensing using nanoparticles," *J. Fluoresc.* **14**(4), 377–389 (2004).
6. K. Aslan, J. Zhang, J. R. Lakowicz, et al., "Saccharide sensing using gold and silver nanoparticles - A review," *J. Fluoresc.* **14**(4), 391–400 (2004).
7. Y. W. C. Cao, R. C. Jin, and C. A. Mirkin, "Nanoparticles with Raman spectroscopic fingerprints for DNA and RNA detection," *Science* **297**(5586), 1536–1540 (2002).
8. Y. Cui, B. Ren, J. L. Yao, et al., "Synthesis of AgcoreAushell bimetallic nanoparticles for immunoassay based on surface-enhanced Raman spectroscopy," *J. Phys. Chem. B* **110**(9), 4002–4006 (2006).
9. K. Aslan, J. R. Lakowicz, and C. D. Geddes, "Nanogold-plasmon-resonance-based glucose sensing," *Anal. Biochem.* **330**(1), 145–155 (2004).
10. M. S. Han, A. K. R. Lytton-Jean, and C. A. Mirkin, "A gold nanoparticle based approach for screening triplex DNA binders," *J. Am. Chem. Soc.* **128**(15), 4954–4955 (2006).
11. M. S. Han, A. K. R. Lytton-Jean, B. K. Oh, et al., "Colorimetric screening of DNA-binding molecules with gold nanoparticle probes," *Angew. Chem., Int. Ed.* **45**(11), 1807–1810 (2006).
12. X. Huang, I. H. El-Sayed, W. Qian, et al., "Cancer cell imaging and photothermal therapy in the near-infrared region by using gold nanorods," *J. Am. Chem. Soc.* **128**(6), 2115–2120 (2006).
13. C. Loo, L. Hirsch, M. H. Lee, et al., "Gold nanoshell bioconjugates for molecular imaging in living cells," *Opt. Lett.* **30**(9), 1012–1014 (2005).
14. K. Sokolov, M. Follen, J. Aaron, et al., "Real-time vital optical imaging of precancer using anti-epidermal growth factor receptor antibodies conjugated to gold nanoparticles," *Cancer Res.* **63**(9), 1999–2004 (2003).
15. K. Sokolov, J. Aaron, B. Hsu, et al., "Optical systems for *in vivo* molecular imaging of cancer," *Technol. Cancer Res. Treat.* **2**(6), 491–504 (2003).
16. K. Aslan, P. Holley, L. Davies, et al., "Angular-ratiometric plasmon-resonance based light scattering for bioaffinity sensing," *J. Am. Chem. Soc.* **127**(34), 12115–12121 (2005).
17. J. Yguerabide and E. E. Yguerabide, "Light-scattering submicroscopic particles as highly fluorescent analogs and their use as tracer labels in clinical and biological applications - I. Theory," *Anal. Biochem.* **262**(2), 137–156 (1998).
18. J. Yguerabide and E. E. Yguerabide, "Light-scattering submicroscopic particles as highly fluorescent analogs and their use as tracer labels in clinical and biological applications - II. Experimental characterization," *Anal. Biochem.* **262**(2), 157–176 (1998).
19. M. J. Abrams and B. A. Murrer, "Metal compounds in therapy and diagnosis," *Science* **261**(5122), 725–730 (1993).
20. J. Malicka, I. Gryczynski, C. D. Geddes, et al., "Metal-enhanced emission from indocyanine green: a new approach to *in vivo* imaging," *J. Biomed. Opt.* **8**(3), 472–478 (2003).
21. R. Shukla, V. Bansal, M. Chaudhary, et al., "Biocompatibility of gold nanoparticles and their endocytotic fate inside the cellular compartment: a microscopic overview," *Langmuir* **21**(23), 10644–10654 (2005).
22. A. Clark, T. Collier, A. Lacy, et al., "Detection of dysplasia with near real time confocal microscopy," *Biomed. Sci. Instrum.* **38**, 393–398 (2002).
23. T. Collier, A. Lacy, R. Richards-Kortum, et al., "Near real-time confocal microscopy of amelanotic tissue: detection of dysplasia in *ex vivo* cervical tissue," *Acad. Radiol.* **9**(5), 504–512 (2002).
24. E. K. Payne, K. L. Shuford, S. Park, et al., "Multipole plasmon resonances in gold nanorods," *J. Phys. Chem. B* **110**(5), 2150–2154 (2006); I. O. Sosa, C. Noguez, and R. G. Barrera, "Optical properties of metal nanoparticles with arbitrary shapes," *J. Phys. Chem. B* **107**(26), 6269–6275 (2003).
25. N. G. Khlebtsov, L. A. Trachuk, and A. G. Mel'nikov, "The effect of the size, shape, and structure of metal nanoparticles on the dependence of their optical properties on the refractive index of a disperse medium," *Opt. Spectrosc.* **98**(1), 77–83 (2005).
26. J. Aaron, N. Nitin, K. Travis, et al., "Plasmon resonance coupling of metal nanoparticles for molecular imaging of carcinogenesis *in vivo*," *J. Biomed. Opt.* **12**(3), 034007 (2007).
27. G. Kim, R. O'Regan, and S. Nie, "Biomedical nanotechnology for molecular imaging, profiling, and drug targeting," *Conf. Proc. IEEE Eng. Med. Biol. Soc.* **1**, 714–716 (2005); D. C. Sullivan and M. Ferrari, "Nanotechnology and tumor imaging: seizing an opportunity," *Mol. Imaging* **3**(4), 364–369 (2004); R. Weissleder, "Scaling down imaging: molecular mapping of cancer in mice," *Nat. Rev. Cancer* **2**(1), 11–18 (2002).
28. C. Sonnichsen, B. M. Reinhard, J. Liphardt, et al., "A molecular ruler based on plasmon coupling of single gold and silver nanoparticles," *Nat. Biotechnol.* **23**(6), 741–745 (2005).
29. E. R. Hsu, E. V. Anslyn, S. Dharmawardhane, et al., "A far-red fluorescent contrast agent to image epidermal growth factor receptor expression," *Photochem. Photobiol.* **79**(3), 272–279 (2004).
30. G. Frens, "Controlled nucleation for regulation of particle-size in monodisperse gold suspensions," *Nature (London), Phys. Sci.* **241**(105), 20–22 (1973).
31. P. C. Lee and D. Meisel, "Adsorption and surface-enhanced Raman of dyes on silver and gold sols," *J. Phys. Chem.* **86**(17), 3391–3395 (1982).
32. Z. S. Pillai and P. V. Kamat, "What factors control the size and shape of silver nanoparticles in the citrate ion reduction method?" *J. Phys. Chem. B* **108**(3), 945–951 (2004).
33. T. Collier, M. Follen, A. Malpica, et al., "Sources of scattering in cervical tissue: determination of the scattering coefficient by confocal microscopy," *Appl. Opt.* **44**(11), 2072–2081 (2005).
34. K. E. Adams, S. Ke, S. Kwon, F. Liang, Z. Fan, Y. Lu, K. Hirschi, M. E. Mawad, M. A. Barry, and E. M. Sevick-Muraca, "Comparison of visible and near-infrared wavelength-excitable fluorescent dyes for molecular imaging of cancer," *J. Biomed. Opt.* **12**(2), 024017 (2007).
35. Z. Cheng, J. Levi, Z. Xiong, O. Gheysens, S. Keren, X. Chen, and S. S. Gambhir, "Near-infrared fluorescent deoxyglucose analogue for tumor optical imaging in cell culture and living mice," *Bioconjugate Chem.* **17**(3), 662–669 (2006).
36. J. W. Chen, M. Querol Sans, A. Bogdanov, Jr., and R. Weissleder, "Imaging of myeloperoxidase in mice by using novel amplifiable paramagnetic substrates," *Radiology* **240**(2), 473–481 (2006).